

# Towards Noninvasive Glucose Monitoring Based on Bioimpedance Grid Sampling Topology

Yicun Liu , Student Member, IEEE, Wan Zhang , Wei Liu , Yi Lu , Xueran Tao , Shiyue Jia , and Dawei Shi , Senior Member, IEEE

**Abstract**—Fluctuations in blood glucose concentration directly influence the body's internal milieu, resulting in altered bioimpedance characteristics. Recognizing the imperative need of continuous blood glucose monitoring for optimized diabetes care, this article explores a novel, noninvasive method leveraging array bioimpedance and graph neural networks. Concretely, we first extract graph-structured data from bioimpedance measurements using the four-electrode acquisition technology and an array electrode. Then, we propose a differential principal neighborhood aggregation (PNA) graph neural network, which integrates differential computation, positional normalization, and PNA, to process the graph-structured data and solve the problem of blood glucose classification. Finally, we evaluate our system with *in vitro* agar simulation experiments, with the goal of accurately identifying glucose concentrations from 0 to 10 g/l. Our model achieved 95.32% accuracy, 95.30% precision, and 95.18% recall through five-fold cross validation, which outperforms current graph neural network algorithms, and shows promising potential for practical applications.

**Index Terms**—Array electrode, bioimpedance, graph neural network (GNN), noninvasive blood glucose monitoring.

## I. INTRODUCTION

OVER 500 million people around the world suffer from diabetes, with numbers expected to increase by 50% by 2045 [1]. A complete cure for diabetes is still an unsolved medical problem, and patients need to pay long-term attention and intervene in their blood glucose changes. Traditional blood

Manuscript received 15 November 2023; revised 31 January 2024; accepted 26 February 2024. Date of publication 15 April 2024; date of current version 7 August 2024. This work was supported in part by the National Key Research and Development Program of China under Grant 2023YFE0204100, and in part by the National Science Foundation of China under Grant 62261160575. (*Corresponding author: Dawei Shi.*)

Yicun Liu, Yi Lu, Shiyue Jia, and Dawei Shi are with the School of Automation, Beijing Institute of Technology, Beijing 100081, China (e-mail: yicunliu@bit.edu.cn; luda@bit.edu.cn; syuejia@bit.edu.cn; daweishi@bit.edu.cn).

Wan Zhang is with the Department of Clinical Laboratory, China-Japan Friendship Hospital, Beijing 100029, China (e-mail: zhangwan@bit.edu.cn).

Wei Liu is with the Department of Endocrinology and Metabolism, Peking University People's Hospital, Beijing 100044, China (e-mail: liuwei03@bjmu.edu.cn).

Xueran Tao is with the School of Mathematics, Beijing Normal University, Beijing 100875, China (e-mail: 201911180118@mail.bnu.edu.cn).

Color versions of one or more figures in this article are available at <https://doi.org/10.1109/TIE.2024.3376798>.

Digital Object Identifier 10.1109/TIE.2024.3376798

glucose detection methods like continuous glucose monitoring and fingertip blood can harm the skin and cause infections, which are unsuitable for long-term blood glucose monitoring [2], [3], [4], [5]. Hence, noninvasive blood glucose monitoring approaches are crucial for prolonged use in patients with diabetes.

Wearable sensors have made noninvasive health monitoring more prevalent [6], [7], [8]. New methods like integrated metabolic calorimetry [9] and ultrawideband radio frequency [10] have improved blood glucose monitoring. However, limited by energy consumption and size, the radio frequency and metabolic thermal methods are challenging to achieve long-term measurements. Thanks to its strong ability to resist interference from environmental changes and continuous acquisition capabilities, spectral technology [11], [12], and electrocardiogram joint measurement technology [13] have received more attention. Nevertheless, motion artifacts and variations in skin color can affect the accuracy of detection and consequently the crowd generalization ability. So, measuring the environmental components within the human body through human tissue impedance spectroscopy is a more effective and intuitive method [14], [15], [16]. The four-electrode impedance measurement method effectively reduces the interference of the contact impedance by adding a pair of measuring electrodes to bypass the impedance contact end [17], [18]. However, the response of the body's bioimpedance is related to the measurement location and the frequency of the emitted excitation stream [19]. Inspired by multipoint deployment strategies to improve blood glucose classification accuracy based on impedance response [20], an array-type impedance acquisition front-end is proposed for flexible adjustment and configuration of measurement frequency and location.

However, the array type of bioimpedance data collected in this study exhibits strong correlations and spatial relevance. The traditional time-series deep learning methods [21], [22], [23], such as long short term neural networks and convolutional neural networks, simply capture the time sequence reliance [21], [22], [23], [24], [25], [26], [27]. Inspired by the application of human behavior recognition with graph neural network (GNN), the spatial information can transform into a topological graph, which shows outstanding performance in extracting topological spatial information in complex data structures [28], [29]. In addition, the principal neighborhood aggregation (PNA) model adopts an aggregation strategy that integrates various aggregators and scale converters, which enhances the ability of the GNN to aggregate the features of surrounding nodes more

comprehensively [30]. Similar topological graph applications combining GNN have become a research hotspot and have been widely adopted in epileptic brain network and alzheimer's disease classification [31], [32], [33], [34], [35]. In this article, based on the four-electrode array bioimpedance collector we designed, complex array data with multifrequency and multi-sampling point changes are collected. To exploit the temporal properties in the data, the array data is topologically processed. The nodes in the topology store the response of each fixed sample point in the multi-frequency collection. Furthermore, the connectivity of edges in the topology is utilized to express the different sample points between nodes. To enhance the signal-to-noise ratio of the bioimpedance signals and reduce interference caused by differences in human tissue structure, a blank differentiation strategy is utilized for the topological impedance array data.

In this article, our goal is to achieve effective blood glucose concentration recognition using the designed four-electrode array impedance acquisition device. The main contributions are as follows.

- 1) Leveraging the four-electrode impedance sensing approach, an array-type bioimpedance acquisition front-end composed of  $4 \times 4$  brass spring probe electrodes is designed to overcome single-point sampling errors, which enables enriched the experiment strategy design. An array electrode selection circuit and frequencies spanning controller is also designed, which provides hardware support for autonomous electrode selection and flexible frequency adjustment.
- 2) A Diff-PNA GNN model is proposed to process the array data, integrating differential processing and position normalization. The proposed model features a differencing step that is employed to eliminate the impedance changes caused by external and internal nonglucose related environmental factors, hence facilitating a concentrated analysis of the intrinsic association between bioimpedance and glycemic indices.
- 3) Given the complexities associated with human experimental procedures, an in vitro hardware-in-the-loop simulation platform of the blood circulatory system of the arm is devised. The platform integrates agar, a glucose solution, and a peristaltic pump, enabling the static and dynamic impedance simulation by varying the agar composition and modulating the glucose solution's flow rate. In the in vitro experiments, the proposed model implemented on the hardware system achieves 95.32% accuracy, 95.30% precision, and 95.18% recall through five-fold cross validation.

The main advantages of the method proposed in this article include the following three aspects. First, the use of differential combination method effectively improves the feature extraction capability of the model for impedance data. Second, the design of array impedance acquisition can realize both single-point impedance measurements and combined traversal measurements on the acquisition surface, which is able to suppress common motion interference and improve data quality to a certain extent in wearable sensing devices. Third, the Diff-PNA model based on the PNA neighborhood aggregation method

has the ability to process the array impedance data, which can continuously aggregate the impedance information at different locations in the array, thus effectively improving the model's performance in blood glucose classification. The experimental results show that Diff-PNA leads to improved performance compared with other methods.

The rest of this article is organized as follows. Section II presents an overview of the proposed noninvasive glucose monitoring framework; Section III introduces the design and implementation of the array-type impedance acquisition system. The proposed Diff-PNA GNN model is introduced in Section IV. The design of the in vitro glucose simulation platform together with the experimental results are presented in Section V. Finally, Section VI concludes this article.

## II. FRAMEWORK OVERVIEW

In this section, a detailed description is provided for the proposed noninvasive blood glucose monitoring method based on bioelectrical impedance. The blood glucose detection problem is simplified as a supervised classification problem, and the model is trained using array impedance data with known blood glucose concentrations to establish the relationship between impedance and blood glucose concentration. The monitoring method consists of two main parts: 1) an array impedance acquisition system for collecting bioelectrical impedance data and 2) a GNN model for describing the relationship between impedance and blood glucose concentration.

Through exploratory data analysis, it is observed that in the absence of blood glucose in blank agar, there are differences in impedance changes among different detection sites with varying excitation frequencies, but no obvious pattern is observed. This suggests the presence of environmental noise and can be explained by the fact that internal and external factors such as blood vessels and muscle tissues significantly impact impedance measurement results, while the changes in bioelectrical impedance caused by blood glucose concentration are relatively subtle. Based on these observations, the bioelectrical impedance acquisition system and data modeling methods are carefully designed, as shown in Fig. 1.

In the impedance acquisition part, a  $4 \times 4$  array of electrodes is used, and an array impedance acquisition strategy is proposed, combining the four-electrode impedance acquisition method to obtain more comprehensive impedance information.

In the data modeling part, the spatial correlation in the array impedance data is considered, and it is reconstructed into graph-structured data to better capture the underlying spatial topological features of impedance. A differential GNN model is proposed, incorporating a 0 g/l sugar aqueous solution to account for environmental noise. By performing differential processing and position normalization on the graphs constructed from the 0 to 10 g/l sugar aqueous and 0 g/l sugar aqueous solutions, the aim is to eliminate noise and minimize errors caused by electrode distance. Finally, the GNN model PNA, which aggregates neighboring nodes, is trained to obtain blood glucose concentration classification results.

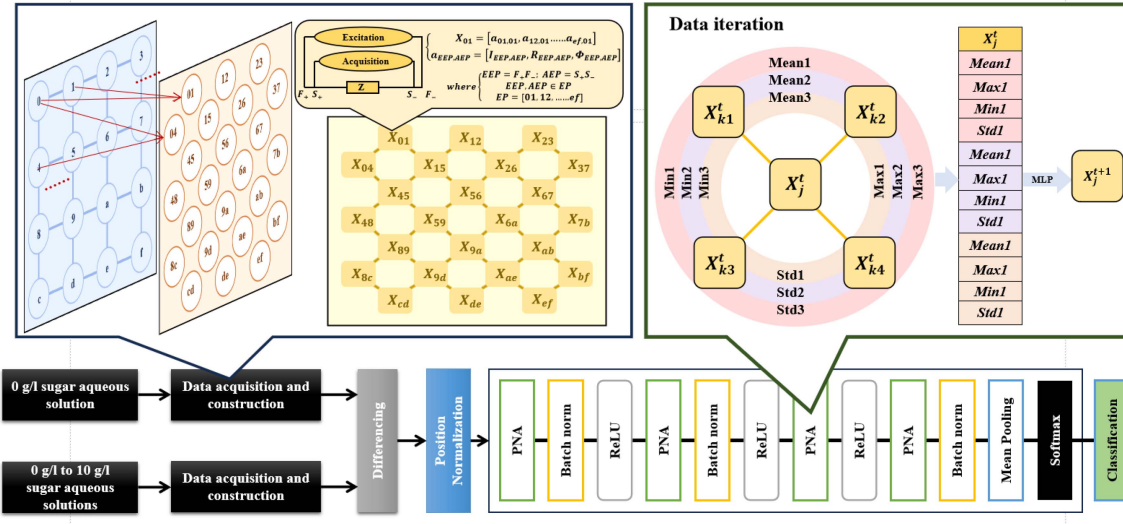


**Fig. 1.** Diagram of the proposed noninvasive blood glucose monitoring framework. The collected impedance data and the blank group impedance data are first reorganized into graph-structured data. Then, they are inputted into the difference layer for feature enhancement. After that, the influence brought by the position is eliminated through position normalization. Finally, the classification problem of blood glucose concentration is solved using a PNA-based graph neural network.

### III. ARRAY TYPE IMPEDANCE ACQUISITION SYSTEM

This section introduces the theoretical background and specific implementation methods of array impedance acquisition.

Biological tissues are composed of a large number of cells with various shapes, which are in turn composed of intracellular and extracellular fluids. In terms of electrical characteristics, the intracellular and extracellular fluids exhibit resistive properties, while the cell membrane exhibits capacitive properties. Therefore, the impedance characteristics of biological tissues vary with the frequency of the applied stimulus signal. Schwan's dispersion theory shows that biological tissues exhibit scattering in three frequency bands:  $\alpha$  (1–100 Hz),  $\beta$  (10 kHz–100 MHz), and  $\gamma$  (greater than 10 MHz). Glucose is distributed in both intracellular and extracellular fluids in biological tissues. Therefore, the frequency range of 10–150 kHz has been selected, which mainly reflects the electrical properties of extracellular and intracellular fluids, for the study of noninvasive blood glucose detection technology.

In the measurement of biological impedance, contact impedance can cause distortion of the excitation voltage waveform, introduce temperature errors, and affect frequency characteristics. Four-electrode impedance measurement effectively reduces the influence of contact impedance by separating the excitation circuit and acquisition circuit. In this work, an array-type electrode is designed with an implementation of four-electrode measurement method for biological impedance acquisition (see Fig. 2). The electrode array comprises 16 spring pins and an arrayed printed circuit board (PCB). The spring pins are constructed with standard brass components, and the electrodes are affixed to the arrayed PCB through welding. Specifically, the array electrode base plate adopts 4 cm  $\times$  4 cm PCB with electrode spacing of 9.5 mm, and an FPC connector with contact 16 and spacing of 0.5 mm. All adjacent electrode pairs (EP) constitute

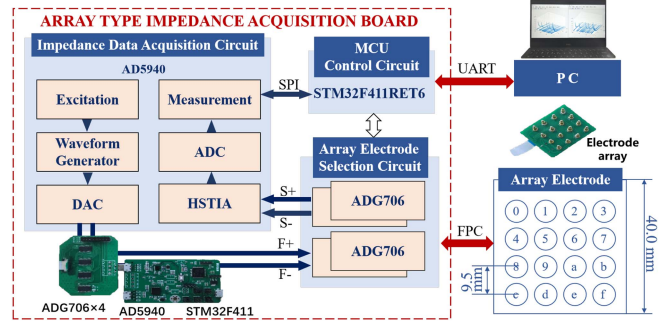


**Fig. 2.** Array impedance acquisition system. The system consists of an arrayed impedance acquisition board, which interacts with the target object through arrayed electrodes, and an impedance acquisition strategy for data acquisition. After the data is acquired, it is communicated to a GPU for model inference and estimation of the blood glucose value of the target object.

an electrode pair group, any pair of which can be chosen as the excitation electrode pair (EEP) or the acquisition electrode pair (AEP). During a complete acquisition cycle, the EPs are initially traversed to obtain the EEP, followed by a subsequent traversal to acquire the activated AEP. Consequently, this acquisition method yields a total of  $24 \times 24$  combination possibilities.

The impedance data acquisition circuit adopts ADI's AD5940, where the excitation circuit ( $F_+$ ,  $F_-$ ) and measurement circuit ( $S_+$ ,  $S_-$ ) are connected to the array electrode selection unit. The array electrode selection unit uses four high-precision 16 channel multiplexers ADG706, with inputs connected to  $F_+$ ,  $F_-$ ,  $S_+$  and  $S_-$ , and outputs connected to 16 electrodes. An STM32 microcontroller (STM32F411RET6) controls the selection of output channels, so as to obtain and transmit array impedance data. A GPU (Nvidia 2080Ti) is utilized for the

deployment of the trained GNN model. This involves structuring the impedance data into an array-based graph data format, followed by employing the data for model inference to determine the current glucose concentration.

#### IV. BLOOD GLUCOSE DETECTION MODEL

##### A. Problem Formulation

In this section, we consider a classification problem of glucose solution concentration based on the impedance data measured by electrode pairs. Specifically, let  $\text{EPs} := \{01, 04, \dots, \text{ef}\}$  denote the set of adjacent EPs. Define the impedance data generated by EPs for one time instant as  $\Pi(\text{EPs})$ , which is the input of the classification problem. In this work, we divide the range of glucose in  $[0, 10.5] \text{ g/l}$  into 11 intervals, namely,  $\mathcal{G} := \{[0, 0.5), [0.5, 1.5), \dots, [9.5, 10.5)\} \text{ g/l}$ , and let  $C \in \mathcal{G}$  denote the output of the classification problem. A data-driven classifier  $f$  is trained to learn the map between  $\Pi$  and  $C$

$$f : \Pi(\text{EPs}) \rightarrow C. \quad (1)$$

The reason of treating the estimation of glucose concentration as a classification problem is that the bioelectrical impedance measurements are subject to nonignorable noises, and therefore accurate regression fitting of glucose concentration based on these noisy measurements has limited practical significance, and may lead to a complicated network structure. Alternatively, it is meaningful to quantify the glucose concentration of sensors into a reasonable number of concentration intervals. By solving a classification problem, we are able to obtain a glucose classifier based on bioelectrical impedance measurements with acceptable accuracy and tolerable computational complexity.

To solve the aforementioned classification problem, a noninvasive blood glucose monitoring framework is proposed based on GNN, as shown in Fig. 1. Specifically, the blood glucose detection procedure comprises three steps. First, the measured array impedance data is converted into graph-structured data, and graph topological features are extracted. Next, the Diff-PNA model is used to embed the transformed data. Lastly, the classifier at the end of the network determines the classification of blood glucose concentration.

##### B. Graph Construction and Data Reorganization

There are 16 array-type electrodes in the designed impedance acquisition system, which motivates us to restructure the array-type impedance data as undirected graph data, as illustrated in Fig. 3(a). The 16 graph nodes correspond to the 16 electrodes, with 24 edges connecting adjacent node pairs designated as electrode pairs. The impedance values serve as edge attributes in the graph.

However, most GNN models inadequately learn edge attributes, resulting in challenges in effectively utilizing impedance information. In addition, in the four-wire resistance measurement method, an electrode pair consists of two electrodes, whereas each node in the current graph represents a single electrode, which does not form a complete impedance excitation or acquisition unit. To address this issue, the original graph

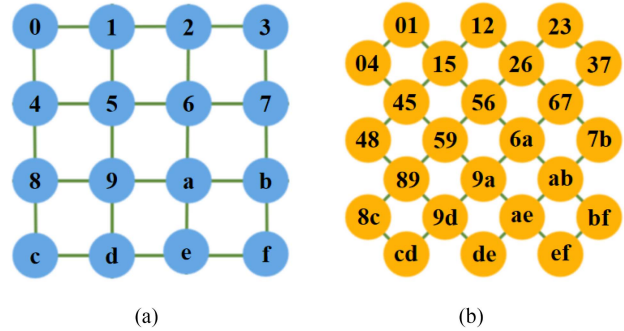


**Fig. 3.** Graph construction and transformation. The left figure is the graph constructed based on the original array electrode structure and the impedance data acquisition mode. The right figure is the new graph structure obtained by transforming the nodes of the original graph into edges and edges into nodes. The edge connecting nodes 0 and 1 in the left figure represents the impedance values of the electrode pairs, and it is converted to node 01 in the right figure. The connections between the other edges and nodes of the two figures are similar. (a) Original graph. (b) Transformed graph.

structure is transformed by merging adjacent nodes capable of forming an electrode pair into a single node, as depicted in Fig. 3(b). This enables the storage of impedance as node attributes, where each node represents an acquisition electrode pair.

The node set of the transformed graph is denoted as  $N$ ,  $N := \{\text{'01'}, \text{'12'}, \dots, \text{'ef'}\}$  (see Fig. 3) and the elements represent the edge of two adjacent nodes in the original graph, e.g., ‘01’ means the edge of the original nodes ‘0’ and ‘1’.  $n$  represents the number of nodes in the graph. The node attribute matrix of the graph is denoted as  $\mathbf{X}$ , which is defined as

$$\mathbf{X} := [\mathbf{I}, \mathbf{R}, \Phi] = (X_1, X_2, \dots, X_j, \dots, X_n)' \quad (2)$$

where  $X_j$  is the attribute of node  $j$ , while  $\mathbf{I}$  represents a directional identity matrix of  $n$ -dimensions utilized to indicate whether the current electrode pair is the stimulating pair. Furthermore,  $\mathbf{R} := [R_{ij}]_{n \times n}$ ,  $\Phi := [\Phi_{ij}]_{n \times n}$  are matrices representing resistance and phase, respectively.  $R_{ij}$ ,  $\Phi_{ij}$  represent the resistance and the phase values when the excitation electrode pair is  $i$  and the acquisition electrode pair is  $j$ , where  $i, j \in N$ .

##### C. Diff-PNA Model

The Diff-PNA model is proposed to address the modeling and classification challenges of array-type impedance graphs. It integrates the idea of PNA with a difference operation and position normalization procedure. This model extracts meaningful features from the graph data using a four-layer PNA network and a classifier at the end of the network determines the category of blood glucose concentration. The aim of this model is to improve performance on the eleven-class classification task of blood glucose concentration.

First, the differencing step is employed to eliminate the impedance changes caused by external and internal environmental factors that are not related to blood glucose. During the step, an empty graph is constructed using array-type impedance data obtained under experimental conditions where simulated

blood vessels and blood glucose are not present. This empty graph effectively captures and quantifies the noise in the data, and its node attribute matrix is denoted as  $\mathbf{X}_{\text{empty}}$ . Next, the empty data graph is subtracted from the experimental data graph at the corresponding stimulation frequency. Considering that impedance values in the empty graph are generally higher than those in the experimental graph, subtracting the empty graph from the experimental graph efficiently avoids the generation of negative values, thus facilitating data analysis. The differenced node attribute matrix is calculated as  $\Delta \mathbf{X} := [\mathbf{I}, \Delta \mathbf{R}, \Delta \Phi] = \mathbf{X}_{\text{empty}} - \mathbf{X} + [\mathbf{I}, \mathbf{O}, \mathbf{O}]$ , where  $\mathbf{O}$  is the  $n \times n$  zero matrix.

A position normalization technique is employed to reduce the impact of inaccurate measurements, as it is assumed that the measured impedance values may increase with increasing distance between excitation and acquisition. This technique involves dividing the elements of the resistance matrix by their corresponding elements in the distance matrix. The distance matrix, denoted as  $\mathbf{H} := [h_{ij}]_{n \times n}$ , represents the Euclidean distance between node  $i$  and  $j$ . In the electrode array, the coordinates are constructed with the node 0 as the coordinate origin and the distance between adjacent nodes as 1. In the converted electrode pair structure, the coordinates of the node pairs are the average of the horizontal and vertical coordinates of the two electrodes. For example,  $h_{01,12} = 1$ . To avoid division by zero, a value of 1 is added to each element of the distance matrix  $\mathbf{H}$ . The specific normalization equation is as follows:

$$\Delta \tilde{\mathbf{R}} := \Delta \mathbf{R} \oslash (\mathbf{H} + \mathbf{1}_n \cdot \mathbf{1}_n^T), \quad (3)$$

$$\Delta \tilde{\Phi} := \text{mod}(\Delta \Phi, 360) \quad (4)$$

where  $\oslash$  represents the Hammond division, which performs division on corresponding elements of the two matrices,  $\mathbf{1}_n$  represents a column vector of length  $n$  with all elements being 1, and  $\text{mod}(a, b)$  is the module operator to obtain a remainder of  $a$  divided by  $b$ .

Next, normalized impedance with position  $\Delta \tilde{\mathbf{R}}_p, \Delta \tilde{\Phi}_p$  are obtained as follows:

$$\Delta \tilde{\mathbf{R}}_p := \Sigma^{-1} (\mathbf{I} - (\mathbf{1}_n \cdot \mathbf{1}_n^T) / n) \Delta \tilde{\mathbf{R}}, \quad (5)$$

$$\Delta \tilde{\Phi}_p := \Sigma^{-1} (\mathbf{I} - (\mathbf{1}_n \cdot \mathbf{1}_n^T) / n) \Delta \tilde{\Phi} \quad (6)$$

where  $\Sigma = \text{diag}(\sigma_1, \sigma_2, \dots, \sigma_n)$ ,  $\sigma_i$  is the standard deviation (SD) of the  $i$ th column of  $\Delta \mathbf{R}$ . The graphs are updated by replacing the node attribute matrix  $\mathbf{X}$  with  $\tilde{\mathbf{X}}_p$ , where  $\tilde{\mathbf{X}}_p := [\mathbf{I}, \Delta \tilde{\mathbf{R}}_p, \Delta \tilde{\Phi}_p]$ . The updated graphs are then fed into a GNN for further processing, as shown in Fig. 1.

The propagation rule of the PNA layer can be described as follows [30]:

$$X^{(0)} := \tilde{\mathbf{X}}_p, \quad (7)$$

$$X_j^{(t+1)} := U \left( X_j^{(t)}, \bigoplus_{(j,k) \in E} X_k^{(t)} \right). \quad (8)$$

Here,  $U$  is a multilayer perceptron that reduces the dimension of the concatenated message (in space  $\mathbb{R}^{13F}$ ) back to  $\mathbb{R}^F$ , where  $F$  is the dimension of features in the network,  $E$  represents the

set of edges in the graph, and

$$\bigoplus := \begin{bmatrix} I \\ S(d, \alpha = 1) \\ S(d, \alpha = -1) \end{bmatrix} \otimes \begin{bmatrix} \mu \\ \sigma \\ \max \\ \min \end{bmatrix} \quad (9)$$

where  $\mu, \sigma, \max, \min$  are four column vectors representing the aggregated results obtained from the neighboring nodes of the  $i$ th node, using four different aggregation methods, namely, mean, standard variance, maximum, and minimum, respectively;  $\otimes$  denotes the Kronecker product;  $S$  is a scalar-valued aggregator operation defined as

$$S(d, \alpha) := (\log(d + 1) / \delta)^\alpha, \quad (10)$$

$$\delta := \frac{1}{n} \sum_{i=1}^n \log(d_i + 1) \quad (11)$$

where  $\delta$  is a normalization parameter computed over the training set,  $d$  is the degree of the node receiving the message, which is a measure of the number of connections or links that a node has with other nodes in a network;  $\alpha$  is a scaling parameter.

After processing PNA layer, a batch normalization layer is applied to normalize the node attributes. In the model proposed in this article, the activation function serves as a nonlinear mapping that maps features from a linearly indivisible space to a linearly divisible space and the typical ReLU( $\cdot$ ) activation function is chosen. A total of four PNA layers are constructed.

To read out the output of network  $\mathbf{X}^{\text{output}}$  and accomplish graph-level classification, the node attribute matrix is passed through a global average pooling layer to compute the average feature across all nodes. As a result, a global feature vector  $\mathbf{g}$  is generated, which captures the collective representation of the entire graph and can be denoted as

$$\mathbf{g} := \frac{1}{n} \sum_{i=1}^n X_i^{\text{output}}. \quad (12)$$

Subsequently, the global feature vector  $\mathbf{g}$  is fed into a classifier for the classification of blood glucose levels. A linear layer coupled with a log-softmax function is employed for the purpose of classification. The model is trained utilizing the cross-entropy loss function, which can be represented mathematically as

$$L := \frac{1}{m} \sum_{j=1}^m \sum_{i=1}^n -y_{ji} \log \hat{y}_{ji} - (1 - y_{ji}) \log(1 - \hat{y}_{ji}) \quad (13)$$

where  $\hat{y}$  denotes the predicted class of the model, and  $m$  corresponds to the batch size of the model.

## V. RESULTS

In this section, the in vitro simulation experiment conducted to acquire labeled array-type impedance data for blood glucose model evaluation is elaborated. The closed liquid circulation system consists of an arm simulation device, an array impedance acquisition device, and glucose solution. Subsequently, this section evaluates and analyzes the performance of the proposed glucose concentration classification model based on the collected impedance data. Before each experiment, the glucose solution

is fully stirred, and the peristaltic pump is used to circulate the solution for one minute before data collection, so as to ensure the glucose solution concentration in the whole system is the same to the greatest extent.

### A. Data Collection Through in Vitro Experiments

The data used in this work are collected through an in vitro simulation experiment. The experiment utilizes acrylic containers, AGAR gels, and poly-concentrated sugar aqueous solutions. The acrylic container, measuring  $200\text{ cm} \times 60\text{ cm} \times 60\text{ cm}$ , simulates the size of a human wrist. It features two 7 mm diameter holes on each side for inserting latex tubes into the AGAR gel. To prepare the AGAR gel, 2% AGAR powder is mixed with distilled water and boiled. Then, 300 ml of the mixture is poured into both the acrylic container and the container with latex tubes. After allowing the gel to set for 6 hours, the latex tube is removed from the latter container, resulting in a pure AGAR gel and a gel with holes. Poly-concentrated sugar aqueous solutions are created by mixing distilled water with glucose at concentrations ranging from 0 to 10 g/l.

The arm simulation device includes a peristaltic pump, sugar solution, acrylic casing, and agarose gel with holes. By controlling the flow rate of the sugar solution with the peristaltic pump, the hemodynamic characteristics of blood are simulated. The agarose gel simulates the static characteristics of arm tissue. Varying the concentration of the sugar solution allows for simulating changes in blood glucose levels. A 0 g/l sugar aqueous solution experiment platform, consisting of sugar solution, acrylic casing, and pure agarose gel, is also set up for comparison. The array-type impedance acquisition device features a frequency-conversion acquisition driver based on array electrodes. Impedance data from the arm simulation device are collected using the array-type electrodes.

Next, the array impedance acquisition system is set up. This involves configuring AD5940 parameters and selecting array electrodes. The four-wire impedance measurement method is adopted, with the excitation frequency logarithmically increasing 50 times between 10 000 Hz and 150 000 Hz. The excitation voltage is set at 600 mV, and the internal calibration resistor at  $1\text{ k}\Omega$ . Electrode pairs are selected by choosing two electrodes with a relative distance of 1 in the horizontal and vertical directions, enabling comprehensive and accurate impedance data collection.

Using the experimental platform and array impedance acquisition system, experiments are conducted to obtain array impedance data. Impedance data from the 0 g/l sugar aqueous solution are collected first, followed by data from the 0 to 10 g/l sugar aqueous solutions. In the arm simulation experimental platform, the peristaltic pump speed is set at 0 r/min and 500 r/min, respectively. The glucose solution concentration is sequentially changed from 0 to 10 g/l, and impedance data at different concentrations are recorded. In total, the 0 g/l sugar aqueous solution experiment yields 50 sets of array impedance data for each of the 50 excitation frequencies, resulting in a total of 50 sets of data. The 0 to 10 g/l sugar aqueous solutions experiment produces 100 sets of data, covering eleven glucose

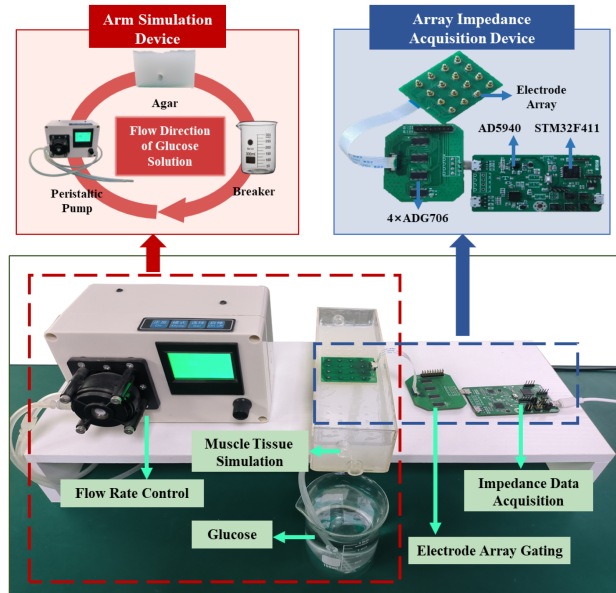


**Fig. 4.** Experiment equipments. This experiment consists of an arm simulation device and an array impedance acquisition device. The prepared glucose solution is first adjusted for flow rate through a peristaltic pump, and then flows through agar with holes to a beaker to simulate blood flow at the arm. The array electrodes of the array impedance collection device are placed on agar to collect variable frequency array impedance data for further analysis.

solution concentrations, 50 excitation frequencies, and 2 flow rates. Therefore, there are 1100 sets of data, with each set containing 576 impedance measurement values corresponding to 24 excitations.

### B. Model Evaluation

To increase the reliability of classification results, a five-fold cross-validated method is employed for the proposed model. The array-type impedance dataset is divided into five subsets, four for training, and the remaining one for testing. At each epoch, the GNN network with current model parameters is used to the testing set to evaluate the generalization performance of the GNN network. This procedure is repeated five times to ensure each subset has an equal chance of being tested. The average performance of the model is presented in Fig. 5.

It can be observed that the training set exhibits better fit than the test set. As the number of epochs increases, the accuracy improves and the loss decreases, reaching a plateau at approximately 50 epochs. The average test accuracy across the five folds is impressive at approximately 95.32%. Evidently, the model demonstrates good generalization ability and converges quickly. Notably, at around 20 epochs, there is a noticeable fluctuation in the accuracy and loss of the test set, indicating that when the number of epochs is too small, the model may fall into local minima, resulting in poor fitting. Therefore, selecting an epoch value of 50 (or greater) promotes greater robustness. In the following, the GNN model obtained at the end of epoch 59 is used for comparison with other classification methods.

To evaluate the performance of a multiclass classification model, the receiver operating characteristic (ROC) curve is

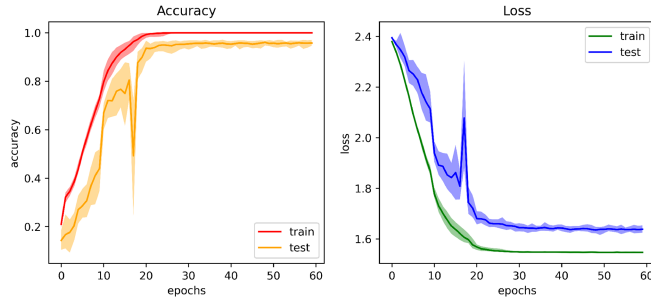


**Fig. 5.** Accuracy and loss in five-fold cross-validation. The shaded areas in the left figure and the right figure reflect the fluctuation range of the accuracy and loss for the training set and test set, respectively. The solid lines represent the mean value of the accuracy and loss over 20 repetitions of the five-fold cross-validation.

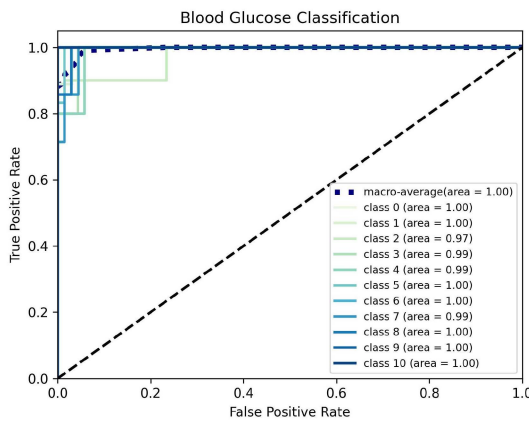


**Fig. 6.** ROC curve. ROC curves are drawn for eleven different blood glucose concentrations and marked with progressive colors.

employed, presenting the relationship between the true positive rate and false positive rate at varying thresholds. For each class, a ROC curve is plotted by considering the class as the positive and the remaining classes as the negative. The final multiclass ROC curve is obtained by averaging these individual curves, providing a comprehensive assessment of the model's performance across all classes. The area under the curve value is calculated to quantitatively measure the model's performance, representing the discrimination ability of the model in distinguishing between different classes. As illustrated in Fig. 6, the ROC curve demonstrates effective performance of the model across all blood glucose levels with minimal variation observed between different classes.

To comprehensively evaluate the performance of the proposed Diff-PNA model, experiments were conducted, comparing it with current state-of-the-art (SOTA) models (namely, GCN [34], GAT [36], GraphSAGE [37], PNA [30]) and the SOTA model with differentials on the array type impedance dataset. The SOTA model preprocessed with differentials was marked with a Diff prefix. In addition, different variable selection approaches in graph construction and the effect of position normalization were discussed. The four evaluation metrics utilized in this work are accuracy, precision, recall, and F1 [23]. The results are presented in Table I.

**TABLE I**  
COMPARISON OF DIFFERENT METHODS

	Method	Accuracy	Precision	Recall	F1-score
Original	GCN	0.7801	0.7641	0.7620	0.7630
	GAT	0.8106	0.7947	0.7998	0.7973
	GraphSAGE	0.5914	0.4769	0.5964	0.5300
	PNA	0.7283	0.6479	0.7203	0.6822
Difference	Diff-GCN	0.9125	0.9078	0.9074	0.9076
	Diff-GAT	0.9327	0.9310	0.9291	0.9301
	Diff-GraphSAGE	0.7482	0.6622	0.7579	0.7068
Proposed	<b>Diff-PNA</b>	<b>0.9532</b>	<b>0.9530</b>	<b>0.9518</b>	<b>0.9524</b>

The bold values indicate the best results among all models in terms of evaluation metrics, and typically, this optimal outcome is achieved by the proposed Diff-PNA model.

**TABLE II**  
COMPARISON OF NODE ATTRIBUTE CHOICES

Method	Node Matrix $\mathbf{X}$	Accuracy	Precision	Recall	F1-score
Diff-PNA-withr	$[\mathbf{I}, \mathbf{R}, \Delta\tilde{\mathbf{R}}_p, \Delta\tilde{\Phi}_p]$	0.9223	0.9100	0.9198	0.9149
Diff-PNA-noi	$[\mathbf{R}, \Delta\tilde{\mathbf{R}}_p, \Delta\tilde{\Phi}_p]$	0.9269	0.9124	0.9223	0.9173
<b>Diff-PNA</b>	$[\mathbf{L}, \Delta\tilde{\mathbf{R}}_p, \Delta\tilde{\Phi}_p]$	<b>0.9532</b>	<b>0.9530</b>	<b>0.9518</b>	<b>0.9524</b>

The bold values indicate the best results among all models in terms of evaluation metrics, and typically, this optimal outcome is achieved by the proposed Diff-PNA model.

The experimental results indicate the improved classification performance of Diff-PNA, compared with all other methods. Besides, it achieves a 22% improvement in accuracy, a 30% improvement in precision, and a 23% improvement in recall, compared to the previous PNA method. This enhancement can be attributed to the calculation of difference in feature extraction and noise handling, allowing the model to better adapt to the characteristics of the array-type impedance dataset. Results from other differential methods also demonstrate that the inclusion of the differential step improves the performance of the model compared to its original state. The differential strategy utilizes relative impedance values, which are independent of the choice of reference concentration in the blank group. For the in vitro experiments, a glucose concentration of 0 g/l is set as the reference. In practical applications, relatively stable blood glucose data, such as fasting blood glucose levels in the morning, can be used as a substitute for a 0 g/l glucose solution as the reference. This allows the proposed model to be effectively applied in blood glucose monitoring. Furthermore, Table I illustrates that, apart from the differential composition calculation method, the network structure utilizing PNA neighbor aggregation can enhance the extraction of array impedance signal features. Continuously aggregating impedance information at various positions in the array can enhance the model's performance in classifying blood glucose.

In addition, the choice of node attribute in graph construction can have an impact on performance. As presented in Table II, the Diff-PNA-withr model enriches the foundational node characteristics of Diff-PNA by integrating features of  $\mathbf{R}$  and  $\Phi$ , while Diff-PNA-noi is delineated by the absence of the current feature within the Diff-PNA-withr framework. The enhanced classification efficacy of Diff-PNA-noi over Diff-PNA-withr highlights

**TABLE III**  
ANALYSIS OF IMPACT OF POSITION NORMALIZATION

	Accuracy		Precision		Recall		F1-score
	Mean	SD	Mean	SD	Mean	SD	Mean
no pos-norm	0.9513	<b>0.0039</b>	0.9498	<b>0.0063</b>	0.9500	<b>0.0062</b>	0.9499
<b>Diff-PNA</b>	<b>0.9532</b>	0.0061	<b>0.9530</b>	0.0085	<b>0.9518</b>	0.0078	<b>0.9524</b>

The bold values indicate the best results among all models in terms of evaluation metrics, and typically, this optimal outcome is achieved by the proposed Diff-PNA model.

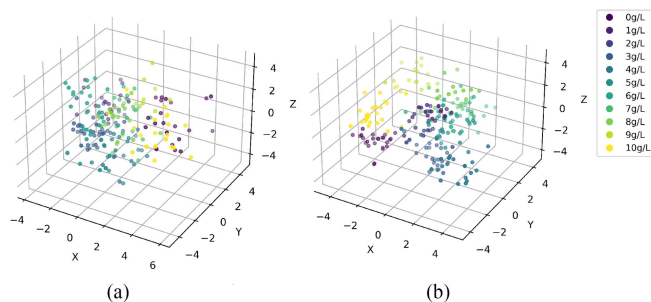


**Fig. 7.** Classification result after PCA dimensionality reduction of the original PNA model and the differenced model. (a) PNA classification. (b) Diff-PNA classification.

the instrumental role of distinctive feature vectors that delineate nodes associated with stimulating versus collecting electrode pairs. Furthermore, the marginal increase in classification accuracy of Diff-PNA over Diff-PNA-noi by 0.0263 indicates that the intrinsic impedance and phase features may harbor noise detrimental to classification accuracy. This revelation affirms the hypothesis that the application of differential steps can be beneficial in mitigating noise within the feature set.

Furthermore, as shown in Table III, when compared to the approach without position normalization, Diff-PNA shows an average performance improvement of 0.19%. This suggests that position normalization can reduce noise in cases where the excitation and acquisition electrodes are far apart. However, it should be noted that the SD increased, which may be due to the loss of information during the normalization process. In summary, our method, Diff-PNA, outperformed others in terms of classification accuracy. For practical implementation, the training of the GNN can be performed offline in a cloud platform, leaving only a tailored version of the GNN on the wearable device, which achieves the fast and effective blood glucose estimation. In extreme cases, both the training and implementation of the GNN can be performed in the cloud, and the embedded system only needs to perform data collection and transmission.

### C. Signal to Noise Ratio Visualization

To facilitate a more intuitive comparison of classification results across different models, the average feature of all nodes in each graph is computed after model training, serving as the graph feature. Subsequently, principal component analysis (PCA) is applied to reduce the dimensionality of the graph feature to a 3-D space. In Fig. 7, the points with different colors represent

the graph data corresponding to different levels of blood glucose concentration. In Fig. 7(a), the points of different colors intersect with each other, just like the yellow and purple points are mixed together, making it difficult for the classifier to accurately distinguish data points with different blood glucose levels, resulting in a higher misclassification rate. In Fig. 7(b), the points of different colors show clear boundaries, e.g., there is a clear demarcation between the yellow and purple points, which allows for easier separation by the classifier and contributes to the accuracy of the classification. It is evident that the data processed by the Diff-PNA model exhibits greater linear separability compared to the data processed by the original PNA model. Therefore, it is hypothesized that the differential step plays a significant role in reducing noise and enhancing the classification accuracy for blood glucose concentration tasks.

## VI. CONCLUSION

In this article, an array type impedance acquisition system based on the four-electrode method was proposed, along with a GNN model Diff-PNA, for noninvasive blood glucose monitoring. The results showed that with this method, the average accuracy, precision, and recall rate achieved through cross-validation were 95.32%, 95.30%, and 95.18%, respectively. These values surpassed other methods such as GCN, GAT, and GraphSAGE. Furthermore, comparative experiments demonstrated the beneficial effects of differential calculations, variable selection in the graph structure, and position normalization in improving the results. In addition, visualization results after PCA dimension reduction indicated that the method effectively addressed the linear separability issue in graph data.

## ACKNOWLEDGMENT

The authors would like to thank the Associate Editor and the anonymous reviewers for their suggestions which have improved the quality of the work.

## REFERENCES

- [1] P. Saeedi et al., "Global and regional diabetes prevalence estimates for 2019 and projections for 2030 and 2045: Results from the international diabetes federation diabetes atlas," *Diabetes Res. Clin. Pract.*, vol. 157, Sep. 2019, Art. no. 107843.
- [2] J. Kropff et al., "Accuracy and longevity of an implantable continuous glucose sensor in the precise study: A 180-day, prospective, multicenter, pivotal trial," *Diabetes Care*, vol. 40, pp. 63–68, Nov. 2016.
- [3] F. Teh et al., "An integrated wearable microneedle array for the continuous monitoring of multiple biomarkers in interstitial fluid," *Nature Biomed. Eng.*, vol. 6, pp. 1–11, May 2022.
- [4] T. Chang et al., "Highly integrated watch for noninvasive continual glucose monitoring," *Microsystems Nanoeng.*, vol. 8, 2022.
- [5] S. Tianyi, Z. Yulong, J. Yanzhen, C. Jung, and L. Jentsai, "Micro interstitial fluid extraction and detection device integrated with the optimal extraction conditions for noninvasive glucose monitoring," *Biosensors Bioelectron.*, vol. 237, Jul. 2023, Art. no. 115515.
- [6] A. Keshet, L. Reicher, N. Bar, and E. Segal, "Wearable and digital devices to monitor and treat metabolic diseases," *Nature Metab.*, vol. 5, pp. 563–571, Apr. 2023.
- [7] C. Yang, C. Garcia, J. Rodriguez-Andina, J. Farina, A. Iniguez, and S. Yin, "Using PPG signals and wearable devices for atrial fibrillation screening," *IEEE Trans. Ind. Electron.*, vol. 66, no. 11, pp. 8832–8842, Nov. 2019.
- [8] P. Y. Chiang, P. C. P. Chao, D. C. Tarn, and C. Y. Yang, "A novel wireless photoplethysmography blood-flow volume sensor for assessing

- arteriovenous fistula of hemodialysis patients," *IEEE Trans. Ind. Electron.*, vol. 64, no. 12, pp. 9626–9635, Dec. 2017.
- [9] D. Wang, "An improved integration sensor of non-invasive blood glucose," in *Proc. 7th IEEE/Int. Conf. Adv. Infocomm Technol.*, 2014, pp. 70–75.
- [10] Z. Wang, X. Xiao, C. Yang, and T. Kikkawa, "Combined approach to estimate blood glucose level in noninvasive monitoring: Ultra-wide band microwave and cascaded general regression neural network," *IEEE Trans. Ind. Informat.*, vol. 18, no. 8, pp. 5105–5114, Aug. 2022.
- [11] A. Prabha, J. Yadav, A. Rani, and V. Singh, "Intelligent estimation of blood glucose level using wristband PPG signal and physiological parameters," *Biomed. Signal Process. Control*, vol. 78, Jun. 2022, Art. no. 103876.
- [12] Y. Yu, J. Huang, J. Zhu, and S. Liang, "An accurate noninvasive blood glucose measurement system using portable near-infrared spectrometer and transfer learning framework," *IEEE Sensors J.*, vol. 21, no. 3, pp. 3506–3519, Feb. 2021.
- [13] J. Li et al., "Noninvasive blood glucose monitoring using spatiotemporal ECG and PPG feature fusion and weight-based choquet integral multi-model approach," *IEEE Trans. Neural Netw. Learn. Syst.*, to be published, doi: [10.1109/TNNLS.2023.3279383](https://doi.org/10.1109/TNNLS.2023.3279383).
- [14] A. Caduff, E. Hirt, Y. Feldman, Z. Ali, and L. Heinemann, "First human experiments with a novel non-invasive, non-optical continuous glucose monitoring system," *Biosensors Bioelectron.*, vol. 19, pp. 209–17, Dec. 2003.
- [15] A. Caduff, F. Dewarrat, M. Talary, G. Stalder, L. Heinemann, and Y. Feldman, "Non-invasive glucose monitoring in patients with diabetes: A novel system based on impedance spectroscopy," *Biosensors Bioelectron.*, vol. 22, pp. 598–604, Jan. 2007.
- [16] C. Martinez, E. Treo, R. Madrid, and C. Felice, "Real-time measurement of glucose using chrono-impedance technique on a second generation biosensor," *Biosensors Bioelectron.*, vol. 29, pp. 200–203, Aug. 2011.
- [17] P. Arpaia, U. Cesaro, M. Frosolone, N. Moccaldi, and M. Tagliafata, "A micro-bioimpedance meter for monitoring insulin bioavailability in personalized diabetes therapy," *Sci. Rep.*, vol. 10, Aug. 2020, Art. no. 13656.
- [18] P. Arpaia, F. Mancino, and N. Moccaldi, "A reproducible bioimpedance transducer for insulin noninvasive measurement," *IEEE Trans. Instrum. Meas.*, vol. 72, 2023, Art. no. 4003811.
- [19] M. Lin, H. Hu, S. Zhou, and S. Xu, "Soft wearable devices for deep-tissue sensing," *Nature Rev. Mater.*, vol. 7, pp. 850–869, Mar. 2022.
- [20] M.-H. Jun et al., "Glucose-independent segmental phase angles from multi-frequency bioimpedance analysis to discriminate diabetes mellitus," *Sci. Rep.*, vol. 8, Jan. 2018, Art. no. 648.
- [21] A. Mohammad-Alikhani, B. Nahid-Mobarakeh, and M.-F. Hsieh, "One-dimensional LSTM-regulated deep residual network for data-driven fault detection in electric machines," *IEEE Trans. Ind. Electron.*, vol. 71, no. 3, pp. 3083–3092, Mar. 2024.
- [22] J. Lv, J. Kuang, Z. Yu, G. Sun, J. Liu, and J. I. Leon, "Diagnosis of PEM fuel cell system based on electrochemical impedance spectroscopy and deep learning method," *IEEE Trans. Ind. Electron.*, vol. 71, no. 1, pp. 657–666, Jan. 2024.
- [23] Y. Tang, L. Zhang, F. Min, and J. He, "Multiscale deep feature learning for human activity recognition using wearable sensors," *IEEE Trans. Ind. Electron.*, vol. 70, no. 2, pp. 2106–2116, Feb. 2023.
- [24] Y. Zhou, J. Li, and M. Dong, "Prediction of actively exerted torque from ankle joint complex based on muscle synergy," *IEEE Trans. Ind. Electron.*, vol. 71, no. 2, pp. 1729–1737, Feb. 2024.
- [25] J. Li, I. Tobore, Y. Liu, A. Kandwal, L. Wang, and Z. Nie, "Non-invasive monitoring of three glucose ranges based on ECG by using DBSCAN-CNN," *IEEE J. Biomed. Health Informat.*, vol. 25, no. 9, pp. 3340–3350, Sep. 2021.
- [26] W. Zhang, Y. Zheng, and Z. Lin, "Real-time gas composition identification and concentration estimation model for artificial olfaction," *IEEE Trans. Ind. Electron.*, to be published, doi: [10.1109/TIE.2023.3306402](https://doi.org/10.1109/TIE.2023.3306402).
- [27] Y. Xing, C. Lv, Y. Liu, Y. Zhao, D. Cao, and S. Kawahara, "Hybrid-learning-based driver steering intention prediction using neuromuscular dynamics," *IEEE Trans. Ind. Electron.*, vol. 69, no. 2, pp. 1750–1761, Feb. 2022.
- [28] H. Lee et al., "Stretchable array electromyography sensor with graph neural network for static and dynamic gestures recognition system," *npj Flexible Electron.*, vol. 7, Apr. 2023.
- [29] R. Zhao, K. Wang, H. Su, and Q. Ji, "Bayesian graph convolution lstm for skeleton based action recognition," in *Proc. IEEE/CVF Int. Conf. Comput. Vis.*, 2019, pp. 6881–6891.
- [30] G. Corso, L. Cavalleri, D. Beaini, P. Liò, and P. Veličković, "Principal neighbourhood aggregation for graph nets," in *Proc. Adv. Neural Inf. Process. Syst.*, 2020, vol. 33, pp. 13260–13271.
- [31] S. F. Storti, I. B. Galazzo, S. Khan, P. Manganotti, and G. Menegaz, "Exploring the epileptic brain network using time-variant effective connectivity and graph theory," *IEEE J. Biomed. Health Informat.*, vol. 21, no. 5, pp. 1411–1421, Sep. 2017.
- [32] F. Gama, A. G. Marques, G. Leus, and A. Ribeiro, "Convolutional neural network architectures for signals supported on graphs," *IEEE Trans. Signal Process.*, vol. 67, no. 4, pp. 1034–1049, Feb. 2019.
- [33] T.-A. Song et al., "Graph convolutional neural networks for Alzheimer's disease classification," in *Proc. IEEE 16th Int. Symp. Biomed. Imag.*, 2019, pp. 414–417.
- [34] F. Monti, D. Boscaini, J. Masci, E. Rodolà, J. Svoboda, and M. M. Bronstein, "Geometric deep learning on graphs and manifolds using mixture model cnns," in *Proc. IEEE Conf. Comput. Vis. Pattern Recognit.*, 2017, pp. 5425–5434.
- [35] R. Levie, F. Monti, X. Bresson, and M. M. Bronstein, "CayleyNets: Graph convolutional neural networks with complex rational spectral filters," *IEEE Trans. Signal Process.*, vol. 67, no. 1, pp. 97–109, Jan. 2019.
- [36] Y. Ye and S. Ji, "Sparse graph attention networks," *IEEE Trans. Knowl. Data Eng.*, vol. 35, no. 1, pp. 905–916, Jan. 2023.
- [37] Y. Cui, C. Shao, L. Luo, L. Wang, S. Gao, and L. Chen, "Center weighted convolution and graphSAGE cooperative network for hyperspectral image classification," *IEEE Trans. Geosci. Remote Sens.*, vol. 61, 2023, Art. no. 5508216.



**Yicun Liu** (Student Member, IEEE) was born in Huanggang, Hubei Province, China. He received the B.Eng. degree in automation from the Taiyuan University of Technology, Shanxi, China, in 2016, and the M.Sc. degree, in 2019, in control science and engineering from the Beijing Institute of Technology, Beijing, China, where he is currently working toward the Eng.D. degree in electronic information.

His research interests include medical signal processing and artificial intelligence algorithm

with applications to wearable smart devices.



**Wan Zhang** received the bachelor's degree in medicine from Shandong University, Jinan, China, in 2010, and the master's degree in clinical medicine diagnostics from the Institute of Clinical Medicine, China-Japan Friendship Hospital, Beijing, China, in 2013.

She is currently a Physician with the Department of Clinical Laboratory, China-Japan Friendship Hospital. Her research interests include clinical diagnostics and noninvasive intelligent sensing of physiological variables.



**Wei Liu** received the bachelor's degree in clinical medicine and the Master's degree in internal medicine from Peking University, Beijing, China, in 2008 and 2013, respectively.

She is a Physician with the Department of Endocrinology, People's Hospital, Peking University. Her main research interests include molecular etiology of diabetes.



**Yi Lu** was born in Taian Shandong Province. He received the bachelor's degree in measurement and control technology and instruments from the Southwestern Jiaotong University, Chengdu, China, in 2021. He is currently working toward the M.Eng. degree in control engineering from the Beijing Institute of Technology, Beijing, China.

His research interests include physiological signal analysis and wearable systems.



**Xueran Tao** was born in Beijing, China. She is currently working toward the B.S. degree in statistics with Beijing Normal University, Beijing, China.

Her research interests include network analysis and graph machine learning.



**Shiyue Jia** was born in Beijing, China. She is currently working toward the B.Eng. degree in automation with the Beijing Institute of Technology, Beijing, China.

Her research interests include intelligent blood glucose prediction and control.



**Dawei Shi** (Senior Member, IEEE) received the B.Eng. degree in electrical engineering and automaton from the Beijing Institute of Technology, Beijing, China, in 2008, and the Ph.D. degree in control systems from the University of Alberta, Edmonton, AB, Canada, in 2014.

He is currently a Professor with the School of Automaton, Beijing Institute of Technology. From 2017 to 2018, he was a Postdoctoral Fellow in bioengineering with Harvard University, Cambridge, MA, USA. His research interests include the analysis and design of advanced sampled-data control systems, with applications to biomedical engineering, robotics, and motion systems.

Dr. Shi is an Associate Editor/Technical Editor for several international journals, including IEEE/ASME TRANSACTIONS ON MECHATRONICS, IEEE TRANSACTIONS ON INDUSTRIAL ELECTRONICS, and *IEEE Control Systems Letters*.